Electronic Supporting Information

Products of the Phenyl Radical (C_6H_5, X^2A_1) - Acetylene (C_2H_2, $X^1\Sigma_g^+$) Reaction in the 800-1,200 K Temperature Range

Oleg V. Kuznetsov,[1] Mikhail M. Evseev,[1] Iakov A. Medvedkov,[1,2] Georgiy I. Tolstov,[1] Nikolay A. Khvatov, Ivan O. Antonov[1], Ralf I. Kaiser[2], Alexander M. Mebel[3], Valeriy N. Azyazov[1]

[1] *Samara National Research University, Samara 443086, Russian Federation.*

[2] *Department of Chemistry, University of Hawai'i at Manoa, Honolulu, HI 96822, USA.*

[3] *Department of Chemistry, Florida International University, Miami, Florida 33199, USA.*

Corresponding to: azyazov@rambler.ru

Table of Contents

Figure S1. Photo of the molecular beam experimental setup at Samara National Research University used in the current study.

Details of Computational Fluid Dynamics (CFD) Simulations

The simulations were conducted using the COMSOL Multiphysics software package, employing the *Heat Transfer in Solids*, the *High Mach Number Laminar Flow* and the *Deformed Geometry* modules. The *Heat Transfer in Solids* module was used to determine temperature profiles within the reactor walls. The *High Mach Number Laminar Flow* module modeled gas flow within the reactor and its expansion into the vacuum chamber. The *Deformed Geometry* module was employed to simulate the operation of the pulsed valve.

Step 1: Wall Temperature Profile Simulation

The initial step involved determining the wall temperature profile by simulating the heating of the reactor's alumina tube, which was equipped with a molybdenum wire heating element. This was achieved using the Heat Transfer in Solids module in COMSOL. The molybdenum wire was modeled as a generalized heat source, and blackbody radiation was accounted for both within the tube and externally from the reactor. The simulated temperature profiles exhibited strong agreement with experimental measurements obtained using a Pt-Rh thermocouple. An example of the calculated reactor wall temperature profile is presented in Figure S2, Panel A. This temperature profile was subsequently utilized as a boundary condition for the subsequent CFD simulations of gas flow.

Step 2: Valve Cycle CFD Simulation

The second step involved CFD simulations of the gas flow during the pulsed valve operation. The mass flow into the reactor was governed by the position of the pulsed valve piston. The simulation of the opening and closing of the valve enabled the use of the reactor's backing pressure as the inlet boundary condition for calculating the mass flow through the valve orifice. The valve piston position was taken as a function of time using a triangular waveform, characterized by a linear rise and decay, with opening and closing times of 60 μs each, resulting in a total simulation time of 120 μs. The maximum valve opening gap was set to 40 μm derived from the data presented in the original work [24] for a supply voltage of -400 V. The gas outflow from the reactor into the vacuum chamber was modeled using a cylindrical volume (5 cm × 5 cm) with an initial pressure of 10^{-2} Torr, attached to the exit of the alumina tube. Representative pressure distributions within the reactor at 20 μs and 70 μs after valve opening are illustrated in Figure S2, Panels B and C.

Step 3: Post-Valve-Closure Gas Outflow Simulation

The final step involved CFD simulations of the gas remaining in the reactor after the pulsed valve was closed. The initial conditions for this step were derived from the final time step of the

valve cycle simulation. The gas outflow into the vacuum was modeled over a period of 500 µs. A representative pressure distribution at 500 µs after valve opening is shown in Figure S2, Panel D.

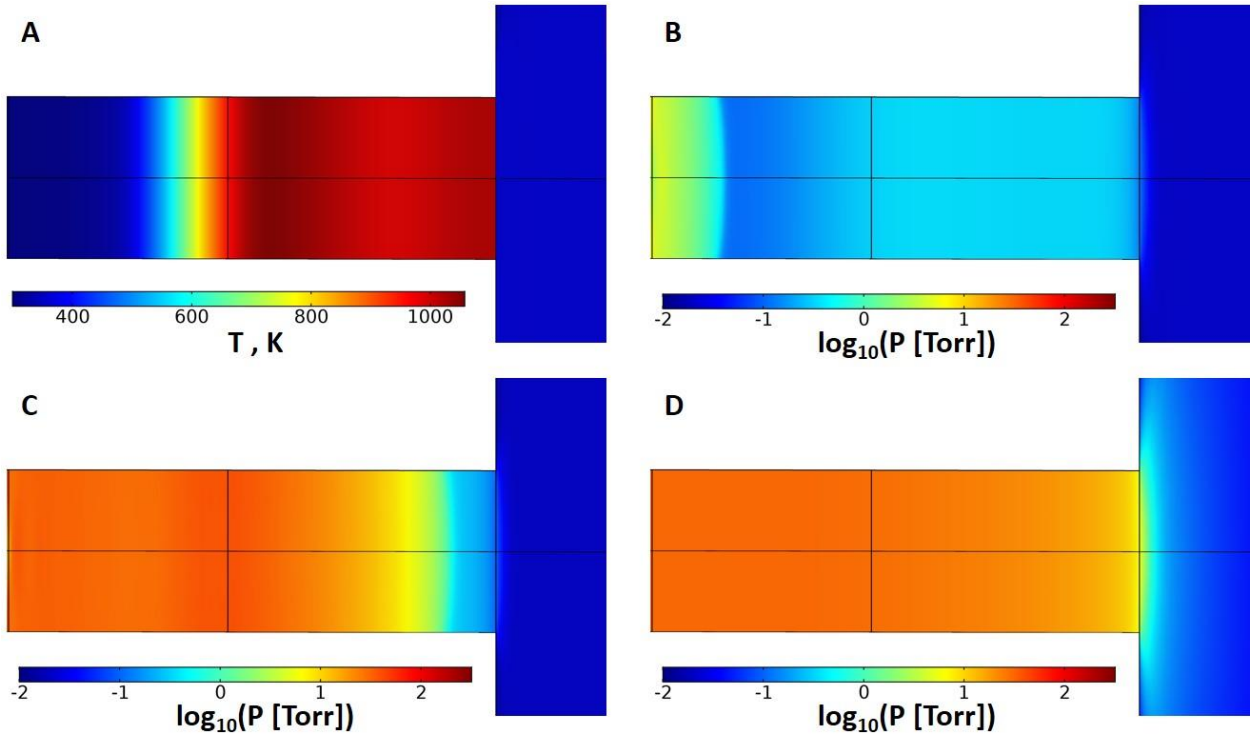

Figure S2. Computational fluid dynamics (CFD) simulation results. (A) Calculated temperature profile of the reactor wall. (B–D) Simulated pressure distributions within the reactor at 20 µs (B), 70 µs (C), and 500 µs (D) following the opening of the pulsed valve, demonstrating the temporal evolution and propagation of the gas pulse.

CFD analysis of microreactor conditions

To investigate the temporal behavior of the gas pulse, we calculated time-dependent mass flows across three cross-sectional areas of the reactor tube. The first area was positioned at the tube entrance, immediately downstream of the pulsed valve nozzle. The second area was located 13.5 mm downstream from the pulsed valve, at the entrance to the heated zone, and the third area was situated 30 mm downstream, at the reactor tube exit.

The calculated mass flows in the three cross-sections, as shown in the top panel of Figure S3, exhibit a bimodal behavior. The first, leading part of the pulse is significantly more intense, with a full width at half maximum (FWHM) duration of 60 µs at the tube entrance, consistent with the opening time of the pulsed valve. As the pulse propagates downstream, its intensity decreases, while its width remains largely unchanged. This behavior is consistent with the gas pulse propagating through the reactor at a well-defined, constant velocity as a coherent entity, while

experiencing gas loss to the walls due to viscous friction. The onset of the leading edge allows for the estimation of the gas pulse velocity. The derived velocity values depend on the backing pressure, ranging from 300 m/s at 100 Torr to 450 m/s at 300 Torr and 550 m/s at 600 Torr.

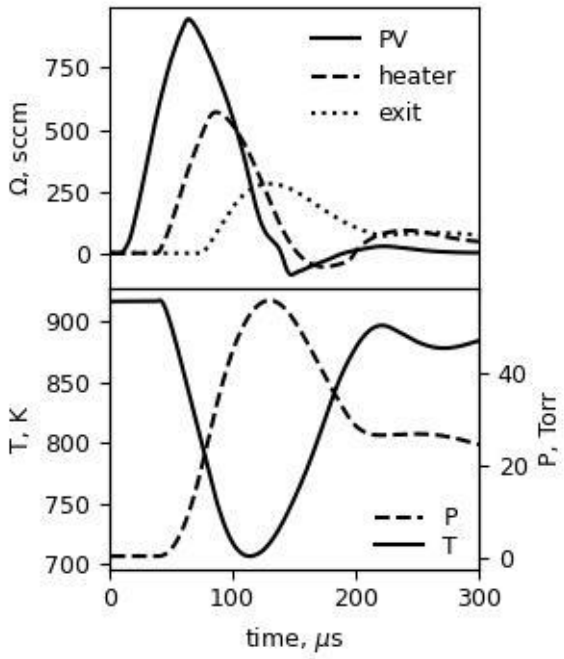

Figure S3. (Top) Simulated integrated mass flows across three key cross-sectional planes of the microreactor tube: PV (pulsed valve exit at 0 mm), heater (entrance of the heated zone at 16.5 mm), and exit (tube outlet at 30 mm). (Bottom) Simulated average temperature and pressure within the heated zone. Simulations were performed under steady-state conditions at p = 300 Torr and T = 1000 K.

The second, trailing part of the pulse exhibits a much longer duration, with temporal behavior consistent with gas left behind the main pulse due to viscous friction along the walls, which slowly leaks from the reactor tube into the vacuum. This trailing part displays wave-like intensity fluctuations, likely caused by shock waves propagating along the tube axis in both directions.

The lower panel of Figure S3 illustrates the time-dependent behavior of temperature and pressure within the microreactor, averaged over the heated volume. It clearly shows a temperature drop and a pressure rise coinciding with the passage of the leading edge of the gas pulse through the heated zone. The magnitude of these changes depends on the backing pressure. For the lowest backing pressure of 100 Torr, the calculations predict a temperature drop (ΔT) of approximately 25 K and a pressure rise (ΔP) of ~12 Torr. At the intermediate backing pressure, the estimated

values are $\Delta T \approx 200$ K and $\Delta P \approx 60$ Torr. For the highest backing pressure of 600 Torr, the predicted changes are $\Delta T \approx 360$ K and $\Delta P \approx 120$ Torr.

CFD simulations were used to determine key experimental conditions in the microreactor's heated zone during gas pulse evolution, including the average residence time, acetylene number density, and average temperature. The residence time was calculated by ensuring equality between the time-integrated mass flows at the entrance and exit cross-sections of the heated zone. Meanwhile, the acetylene number density and temperature were spatially averaged over the entire heated zone volume. The resulting values are summarized in Table 1 in the main text.

Microreactor construction

The high temperature chemical microreactor used in the experimental setup consists of a 3cm long and 1 mm in diameter Al_2O_3 tube, mounted in a stainless steel body. A molybdenum wire is winded around the tube and is used for resistive heating. The wire is fixed on the tube with a high temperature glue. The wire's winding has a small gap in the heating zone to house a type K thermocouple, that is used for measuring the tube wall temperature.

The temperature profile of the reactor tube was measured with a Pt-Rh, by dragging it along the inside wall of the tube and recording the temperature at set intervals. A representative temperature profile is presented on Figure S4.

We have also measured the dependence of average temperature in the heating zone on power, and how the average heat zone temperature correlates to the wall temperature measured by the external type K thermocouple. These dependencies are depicted on Figures S5 and S6.

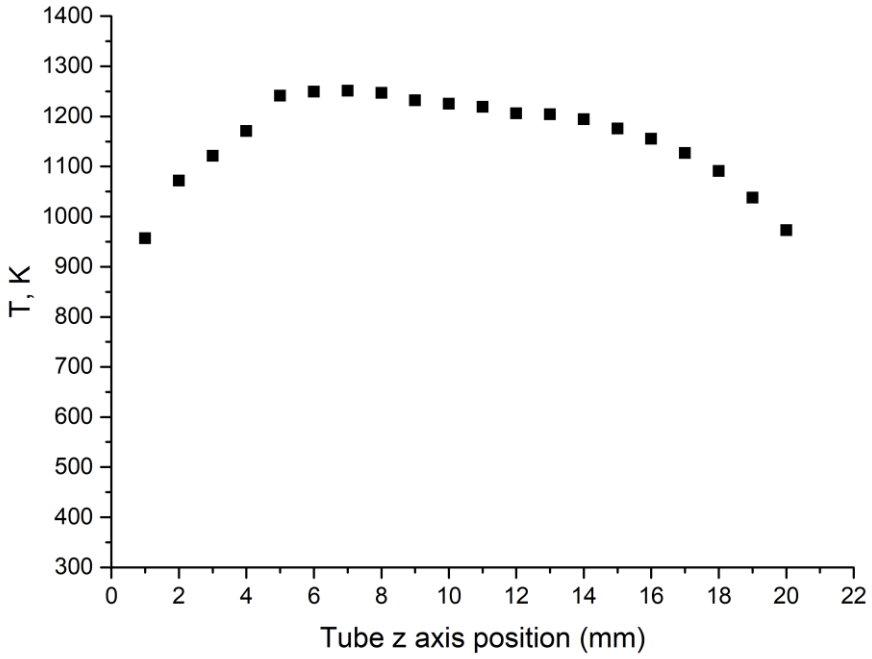

Figure S4. Microreactor tube temperature profile

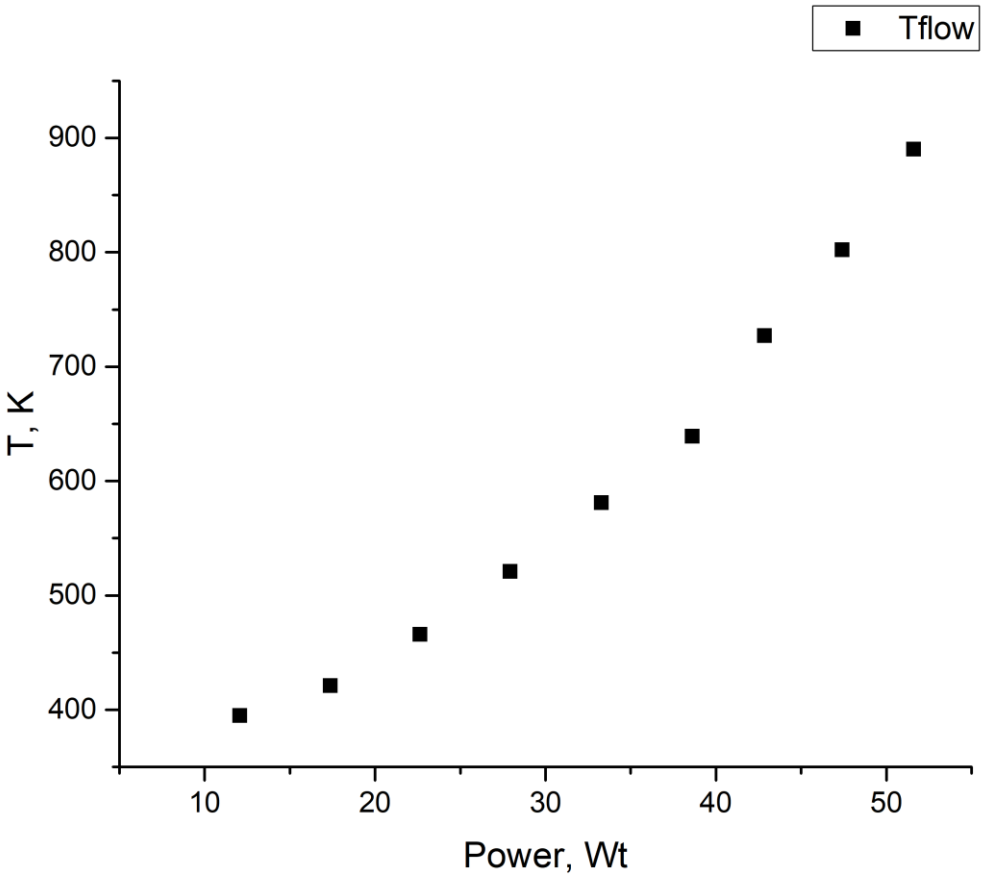

Figure S5. Average temperature in the heated zone as function of heater power

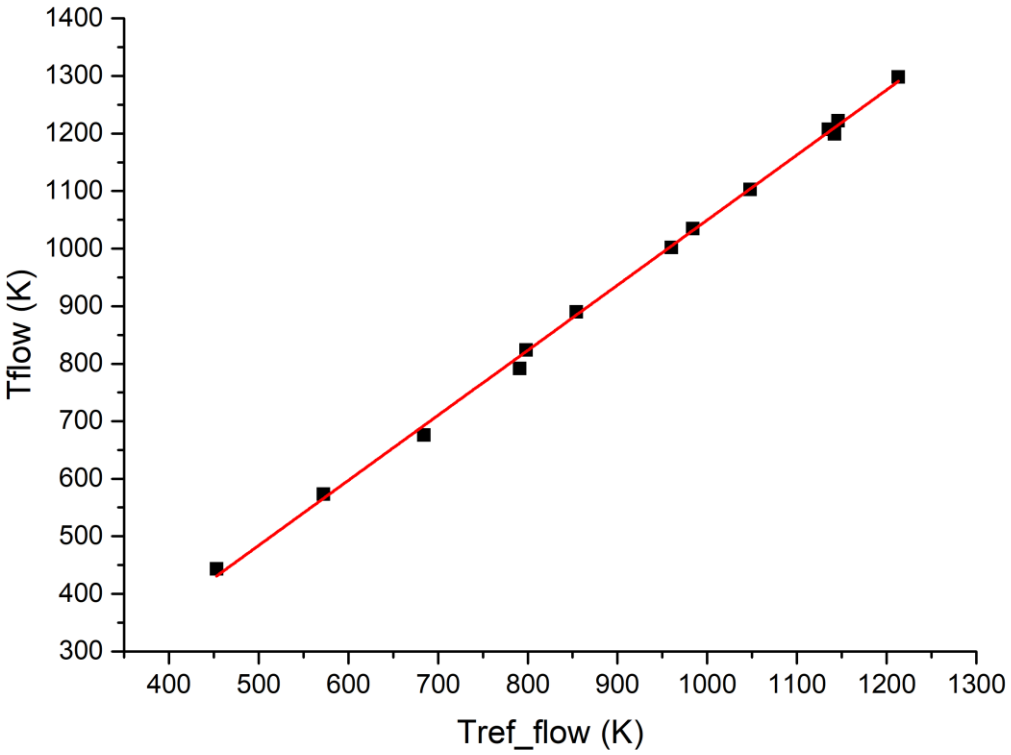

Figure S6. The relationship between the average wall temperature in the heated zone, and the temperature measured with an external thermocouple.

Semi-quantitative analysis of the m/z = 28 signal

The observed m/z = 28 signal at 10.5 eV is noticeable and hence, we carefully considered its potential impact. A quantitative analysis is not feasible with the current data, but we provide below a semi-quantitative assessment explaining why its chemistry does not interfere with the primary conclusions of this work. A direct comparison of the $C_2H_4^+$ and $C_2H_2^+$ signal intensities is misleading due to their drastically different ionization mechanisms. Acetylene (C_2H_2, IP = 11.4 eV) cannot be ionized by a single 10.5 eV photon. The signal at m/z = 26 is attributed to weak multiphoton ionization or, more likely, electron-impact ionization by stray electrons generated from the photoionization of other species/ejected from metal surfaces by stray VUV photons. This is an inherently inefficient and non-quantitative process.

Ethylene (C_2H_4, IP = 10.5 eV) has an ionization energy very close to the laser photon energy. While its single-photon ionization cross-section at 10.5 eV is small, it is still a direct and far more efficient process than the indirect ionization of acetylene. Therefore, a much larger signal for ethylene than acetylene is expected, even if acetylene is orders of magnitude more abundant.

Operating at an energy so close to the ionization threshold presents a significant challenge for quantification. The photoionization cross-section for ethylene in this region is not only small but also highly sensitive to the internal energy (vibrational and rotational temperature) of the molecule. The rotational and especially vibrational cooling in the supersonic expansion after the heated microreactor is incomplete and pressure-dependent, making it impossible to apply a single, well-defined cross-section value for accurate quantification.

Despite the challenges above, we can estimate an upper limit for the ethylene concentration. By comparing the integrated and cross-section-corrected signal of m/z = 28 to that of a known reference species (phenylacetylene, m/z = 102), we estimate that the ethylene concentration is no more than ~10 times that of the phenyl radical precursor (C_6H_5NO). This places it in the range of a significant impurity but still at a concentration that is ~2-3 orders of magnitude lower than the acetylene carrier gas ($[C_2H_2] \approx 5\times10^{16}$ - 5×10^{18} cm^{-3}).

Most importantly, we find no evidence that ethylene participates in chemistry that would compromise this study. Its concentration remains stable, showing no observable consumption within the microreactor; its temporal profile matches that of other stable species like NO. Furthermore, we do not detect any prominent reaction products (e.g., ethylbenzene, styrene) that would be characteristic of significant phenyl radical + ethylene chemistry. The dominant pathways observed forming phenylacetylene and naphthalene are unequivocally attributed to the reaction of phenyl radicals with the vast excess of acetylene, consistent with the HACA mechanism.

In conclusion, while ethylene is present as an impurity, its concentration is negligible compared to acetylene, and the data provide no indication that it influences the key product channels under investigation. Therefore, we are confident that the presence of ethylene does not alter the interpretation of the results concerning the phenyl + acetylene reaction.